

Using computational fluid dynamic/rigid body dynamic results to generate aerodynamic models for projectile flight simulation

M Costello^{1*} and J Sahu²

¹School of Aerospace Engineering, Georgia Institute of Technology, Atlanta, Georgia, USA

²Weapons and Materials Research Directorate, US Army Research Laboratory, Maryland, USA

The manuscript was received on 29 October 2007 and was accepted after revision for publication on 23 June 2008.

DOI: 10.1243/09544100JAERO304

Abstract: A method to efficiently generate a complete aerodynamic description for projectile flight dynamic modelling is described. At the core of the method is an unsteady, time accurate computational fluid dynamic simulation that is tightly coupled to a rigid projectile flight dynamic simulation. A set of short time snippets of simulated projectile motion at different Mach numbers is computed and employed as baseline data. For each time snippet, aerodynamic forces and moments and the full rigid body state vector of the projectile are known. With time synchronized air loads and state vector information, aerodynamic coefficients can be estimated with a simple fitting procedure. By inspecting the condition number of the fitting matrix, it is straightforward to assess the suitability of the time history data to predict a selected set of aerodynamic coefficients. The technique is exercised on an exemplar fin-stabilized projectile with good results.

Keywords: projectile, flight simulation, computational fluid dynamics

1 INTRODUCTION

Four basic methods to predict aerodynamic forces and moments on a projectile in atmospheric flight are commonly used in practice: empirical methods, wind tunnel testing, computational fluid dynamic (CFD) simulation, and spark range testing. Empirical methods have been found very useful in conceptual design of projectiles where rapid and inexpensive estimates of aerodynamic coefficients are needed. These techniques aerodynamically describe the projectile with a set of geometric properties (diameter, number of fins, nose type, nose radius, etc.) and catalog aerodynamic coefficients of many different projectiles as a function of these features. This data is fit to multi-variable equations to create generic models for aerodynamic coefficients as a function of these basic projectile geometric properties. The database of aerodynamic coefficients as a function of projectile features is typically obtained from wind tunnel or spark range tests. This approach

to projectile aerodynamic coefficient estimation is used in several software packages including Missile DATCOM, PRODAS, and AP98 [1–6]. The advantage of this technique is that it is a general method applicable to any projectile. However, it is the least accurate method of the four methods mentioned above, particularly for new configurations that fall outside the realm of projectiles used to form the basic aerodynamic database. Wind tunnel testing is often used during projectile development programs to converge on fine details of the aerodynamic design of the shell [7, 8]. In wind tunnel testing, a specific projectile is mounted in a wind tunnel at various angles of attack with aerodynamic forces and moments measured at various Mach numbers using a sting balance. Wind tunnel testing has the obvious advantage of being based on direct measurement of aerodynamic forces and moments on the projectile. It is also relatively easy to change the wind tunnel model to allow detailed parametric effects to be investigated. The main disadvantage to wind tunnel testing is that it requires a wind tunnel and as such is modestly expensive. Furthermore, dynamic derivatives such as pitch and roll damping as well as Magnus force and moment coefficients are difficult to obtain in a wind tunnel and

*Corresponding author: School of Aerospace Engineering, Georgia Institute of Technology, Atlanta, Georgia 30332, USA. email: mark.costello@ae.gatech.edu

require a complex physical wind tunnel model. Over the past couple of decades, tremendous strides have been made in the application of CFD to prediction of aerodynamic loads on air vehicles, including projectiles. These methods are increasingly being used throughout the weapon development cycle including early in a program to create relatively low cost estimates of aerodynamic characteristics and later in a program to supplement and reduce expensive experimental testing. In CFD simulation, the fundamental fluid dynamic equations are numerically solved for a specific configuration. The most sophisticated computer codes are capable of unsteady time accurate computations using the Navier–Stokes equations. Examples of these tools include, for example, CFD++, Fluent, and Overflow-D. CFD is computationally expensive, requires powerful computers to obtain results in a reasonably timely manner, and requires dedicated engineering specialists to drive these tools [9–24]. Spark range aerodynamic testing has long been considered the gold standard for projectile aerodynamic coefficient estimation. It is the most accurate method for obtaining aerodynamic data on a specific projectile configuration. In spark range aerodynamic testing, a projectile is fired through an enclosed building. At a discrete number of points during the flight of the projectile (<30) the state of the projectile is measured using spark shadowgraphs [25–29]. The projectile state data is subsequently fit to a rigid six-degree-of-freedom projectile model using the aerodynamic coefficients as the fitting parameters [30]. While this technique is the most accurate method for obtaining aerodynamic data on a specific projectile configuration, it is usually the most expensive alternative, requires a spark range facility, and strictly speaking is only valid for the specific projectile configuration tested. More recently, aerodynamic parameters have been estimated using a combination of radar data and on-board instrumentation [31, 32].

Various researchers have used CFD to estimate aerodynamic coefficient estimation of projectiles. Early work focused on Euler solvers applied to steady flow problems while more recent work has solved the Reynolds-averaged Navier–Stokes equations (RANS) and large eddy simulation Navier–Stokes equations for both steady and unsteady conditions [9–24]. For example, to predict pitch damping Weinacht prescribed projectile motion to mimic a typical pitch damping wind tunnel test in a CFD simulation to estimate the different components of the pitch damping coefficient of a fin-stabilized projectile [33]. Excellent agreement between computed and measured pitch damping was attained. Algorithm and computing advances have also led to coupling of CFD codes to projectile rigid body dynamic (RBD) codes for simulation of free flight motion of a projectile in a time accurate manner. Aerodynamic forces and moments

are computed with the CFD solver while the free flight motion of the projectile is computed by integrating the RBD equations of motion. Sahu achieved excellent agreement between spark range measurements and a coupled CFD/RBD approach for a finned stabilized projectile [34]. Projectile position and orientation at down range locations consistent with a spark range test were extracted from the output of the CFD/RBD software to compute aerodynamic coefficients. Standard range reduction software was utilized for this purpose with good agreement obtained when contrasted against example spark range results. The ability to accurately compute projectile aerodynamics in highly unsteady conditions has led to the notion of “virtual wind tunnels” and “virtual fly outs” where the simulation tools above are used to replicate a wind tunnel or spark range test.

Computation time for accurate coupled CFD/RBD simulation remains exceedingly high and does not currently represent a practical method for typical flight dynamic analysis such as impact point statistics (CEP) computation where thousands of fly outs are required. Furthermore, this type of analysis does not allow the same level of understanding of the inherent underlying dynamics of the system that RBD analysis using aerodynamic coefficients yields. However, the coupled CFD/RBD approach does offer an indirect way to rapidly compute the aerodynamic coefficients needed for rigid six-degree-of-freedom simulation. During a time accurate CFD/RBD simulation, aerodynamic forces and moments and the full rigid body state vector of the projectile are generated at each time step in the simulation [34]. This means that aerodynamic forces, aerodynamic moments, position of the mass center, body orientation, translational velocity, and angular velocity of the projectile are all known at the same time instant. With time synchronized air load and state vector information, the aerodynamic coefficients can be estimated with a simple fitting procedure. This paper creates a method to efficiently generate a complete aerodynamic model for a projectile in atmospheric flight using four short-time histories at each Mach number of interest with an industry standard time accurate CFD/RBD simulation. The technique is exercised on example CFD/RBD data for a small fin-stabilized projectile.

2 PROJECTILE CFD/RBD SIMULATION

2.1 Rigid body dynamics

The projectile CFD/RBD algorithm employed here combines a rigid six-degree-of-freedom projectile flight dynamic model with a three-dimensional, time accurate CFD simulation. The RBD dynamic

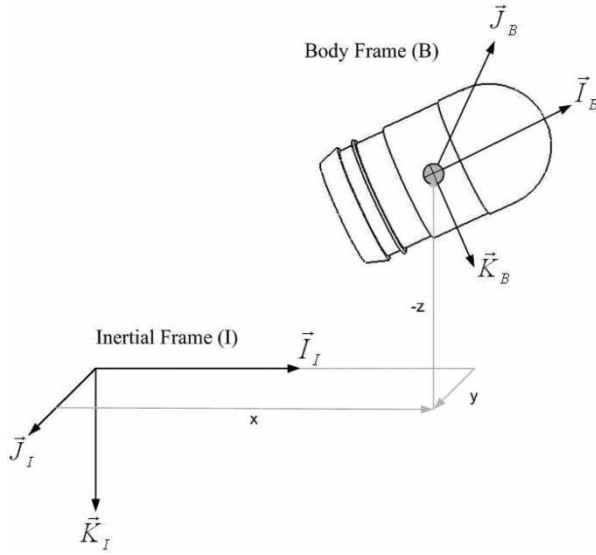


Fig. 1 Reference frame and position definitions

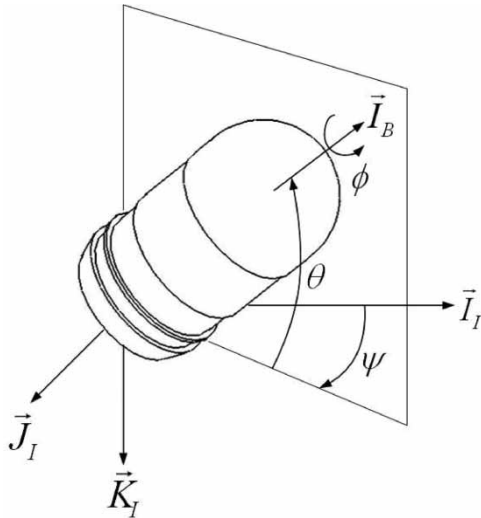


Fig. 2 Projectile orientation definitions

equations are integrated forward in time where aerodynamic forces and moments that drive motion of the projectile are computed using the CFD algorithm. The RBD projectile model allows for three translation degrees of freedom and three rotation degrees of freedom. As shown in Figs 1 and 2, the I frame is attached to the ground while the B frame is fixed to the projectile with the \vec{I}_B axis pointing out the nose of the projectile and the \vec{J}_B and \vec{K}_B unit vectors forming a right handed triad. The projectile state vector is comprised of the inertial position components of the projectile mass center (x, y, z), the standard aerospace sequence Euler angles (ϕ, θ, ψ), the body frame components of the projectile mass center velocity (u, v, w), and the body frame components of the projectile angular velocity vector (p, q, r).

Both the translational and rotational dynamic equations are expressed in the projectile body reference frame. The standard rigid projectile, body frame equations of motion are given by equations (1) through (4) [35]

$$\begin{Bmatrix} \dot{x} \\ \dot{y} \\ \dot{z} \end{Bmatrix} = \begin{bmatrix} c_\theta c_\psi & s_\phi s_\theta c_\psi - c_\phi s_\psi & c_\phi s_\theta c_\psi + s_\phi s_\psi \\ c_\theta s_\psi & s_\phi s_\theta s_\psi + c_\phi c_\psi & c_\phi s_\theta s_\psi - s_\phi c_\psi \\ -s_\theta & s_\phi c_\theta & c_\phi c_\theta \end{bmatrix} \times \begin{Bmatrix} u \\ v \\ w \end{Bmatrix} \quad (1)$$

$$\begin{Bmatrix} \dot{\phi} \\ \dot{\theta} \\ \dot{\psi} \end{Bmatrix} = \begin{bmatrix} 1 & s_\phi t_\theta & c_\phi t_\theta \\ 0 & c_\phi & -s_\phi \\ 0 & s_\phi/c_\theta & c_\phi/c_\theta \end{bmatrix} \begin{Bmatrix} p \\ q \\ r \end{Bmatrix} \quad (2)$$

$$\begin{Bmatrix} \dot{u} \\ \dot{v} \\ \dot{w} \end{Bmatrix} = \begin{Bmatrix} X/m \\ Y/m \\ Z/m \end{Bmatrix} - \begin{bmatrix} 0 & -r & q \\ r & 0 & -p \\ -q & p & 0 \end{bmatrix} \begin{Bmatrix} u \\ v \\ w \end{Bmatrix} \quad (3)$$

$$\begin{Bmatrix} \dot{p} \\ \dot{q} \\ \dot{r} \end{Bmatrix} = [I]^{-1} \begin{Bmatrix} L \\ M \\ N \end{Bmatrix} - \begin{bmatrix} 0 & -r & q \\ r & 0 & -p \\ -q & p & 0 \end{bmatrix} [I] \begin{Bmatrix} p \\ q \\ r \end{Bmatrix} \quad (4)$$

In equations (1) and (2), the shorthand notation $s_\alpha = \sin(\alpha)$, $c_\alpha = \cos(\alpha)$, and $t_\alpha = \tan(\alpha)$. Note that the total applied force components (X, Y, Z) and moment components (L, M, N) contain contributions from weight and aerodynamics. The aerodynamic portion of the applied loads in equations (3) and (4) is computed using the CFD simulation and passed to the RBD simulation.

2.2 CFD solution technique

On the other hand, the CFD flow equations are integrated forward in time where the motion of the projectile that drives flow dynamics are computed using the RBD algorithm. The complete set of three-dimensional time-dependent Navier–Stokes equations is solved in a time-accurate manner for simulation of free flight. The commercially available code, CFD++ is used for the time-accurate unsteady CFD simulations [36, 37]. The basic numerical framework in the code contains unified-grid, unified-physics, and unified-computing features. The three-dimensional time-dependent RANS equations are solved using the following finite volume equation

$$\frac{\partial}{\partial t} \int_V W dV + \oint (F - G) dA = \int_V H dV \quad (5)$$

where \mathbf{W} is the vector of conservative variables, \mathbf{F} and \mathbf{G} are the inviscid and viscous flux vectors, respectively, \mathbf{H} is the vector of source terms, V is the cell volume, and A is the surface area of the cell face. A second-order discretization is used for the flow variables and the turbulent viscosity equation. The turbulence closure is based on topology-parameter-free formulations and turbulence modelling thus, becomes a critical element in the calculation of turbulent flows that are of interest here. Two-equation higher-order RANS turbulence models are used for the computation of turbulent flows. These models are ideally suited to unstructured book-keeping and massively parallel processing due to their independence from constraints related to the placement of boundaries and/or zonal interfaces. Higher order turbulence models are generally more accurate and are widely used. A widely used turbulence model for practical applications is the two-equation k - ε model [38] shown below

$$\frac{d(\rho k)}{dt} = \nabla \cdot \left[\left(\mu + \frac{\mu_t}{\sigma_k} \right) \nabla k \right] + P_k - \rho \varepsilon \quad (6)$$

$$\frac{d(\rho \varepsilon)}{dt} = \nabla \cdot \left[\left(\mu + \frac{\mu_t}{\sigma_\varepsilon} \right) \nabla \varepsilon \right] + (C_{\varepsilon 1} P_k - C_{\varepsilon 2} \rho \varepsilon + E) T_t^{-1} \quad (7)$$

where k is the turbulence kinetic energy, ε is the turbulence dissipation rate, and μ_t is the turbulence eddy viscosity which is a function of k and ε ; P_k is a production term, E is a source term, and T_t is a realizable time scale. Even more sophisticated turbulence modelling such as the 'large eddy simulation' (LES) exists but are prohibitively expensive for practical problems. Recently, hybrid models known as hybrid RANS/LES [39] have been developed that combine the best features of both RANS and LES methods based on local grid resolution. The RANS part is still based on the k - ε model and is used for the most of the flow domain including the turbulent boundary layer region and LES is used in the wake, for example. The hybrid RANS/LES model is generally more suitable for computation of unsteady flow fields especially at transonic and subsonic speeds. For the computation of supersonic flows that are of interest in this research, the two-equation k - ε model described above is adequate. It has been successfully used with good results on a number of projectile aerodynamic applications [19, 24, 34]. These turbulence equations are solved all the way to the wall and generally require fine meshes near the wall surface.

A dual time-stepping approach is used to integrate the flow equations to achieve the desired time-accuracy. The first is an 'outer' or global (and physical) time step that corresponds to the time discretization

of the physical time variation term. This time step can be chosen directly by the user and is typically set to a value to represent one-hundredth of the period of oscillation expected or forced in the transient flow. It is also applied to every cell and is not spatially varying. An artificial or 'inner' or 'local' time variation term is added to the basic physical equations. This time step and corresponding 'inner-iteration' strategy is chosen to help satisfy the physical transient equations to the desired degree. For the inner iterations, the time step is allowed to vary spatially. Also, relaxation with multi-grid (algebraic) acceleration is employed to reduce the residues of the physical transient equations. It is found that an order of magnitude reduction in the residues is usually sufficient to produce a good transient iteration.

2.3 CFD/RBD coupling and initial conditions

The projectile in the coupled CFD/RBD simulation along with its grid moves and rotates as the projectile flies downrange. Grid velocity is assigned to each mesh point. This general capability can be tailored for many specific situations. For example, the grid point velocities can be specified to correspond to a spinning projectile. In this case, the grid speeds are assigned as if the grid is attached to the projectile and spinning with it. Similarly, to account for RBDs, the grid point velocities can be set as if the grid is attached to the rigid body with six degrees of freedom. As shown in Fig. 2, the six degrees of freedom comprises of the inertial position components of the projectile mass center (x, y, z) and the three standard Euler angles (ϕ, θ, ψ), roll angle, pitch angle, and yaw angle, respectively. For the RBDs, the coupling refers to the interaction between the aerodynamic forces/moments and the dynamic response of the projectile/body to these forces and moments. The forces and moments are computed every CFD time step and transferred to a six-degree-of-freedom module which computes the body's response to the forces and moments. The response is converted into translational and rotational accelerations that are integrated to obtain translational and rotational velocities and integrated once more to obtain linear position and angular orientation. From the dynamic response, the grid point locations and grid point velocities are set.

In order to properly initialize the CFD simulation, two modes of operation for the CFD code are utilized, namely, an uncoupled and a coupled mode. The uncoupled mode is used to initialize the CFD flow solution while the coupled mode represents the final time accurate coupled CFD/RBD solution. In the uncoupled mode, the RBDs are specified. The uncoupled mode begins with a computation performed in 'steady state mode' with the grid

velocities prescribed to account for the proper initial position (x_0, y_0, z_0) , orientation $(\phi_0, \theta_0, \psi_0)$, and translational velocity (u_0, v_0, w_0) components of the complete set of initial conditions to be prescribed. After the steady state solution is converged, the initial spin rate (p_0) is included and a new quasi-steady state solution is obtained using time-accurate CFD. A sufficient number of time steps are performed so that the angular orientation for the spin axis corresponds to the prescribed initial conditions. This quasi-steady state flow solution is the starting point for the time-accurate coupled solution. For the coupled solution, the mesh is translated back to the desired initial position (x_0, y_0, z_0) and the remaining angular velocity initial conditions (q_0, r_0) are then added. In the coupled mode, the aerodynamic forces and moments are passed to the RBD simulation which propagates the rigid state of the projectile forward in time.

3 FLIGHT DYNAMIC PROJECTILE AERODYNAMIC MODEL

The applied loads in equations (3) and (4) contain contributions from projectile weight and body aerodynamic forces and moments as shown below

$$\begin{Bmatrix} X \\ Y \\ Z \end{Bmatrix} = W \begin{Bmatrix} -s_\theta \\ s_\phi c_\theta \\ c_\phi c_\theta \end{Bmatrix} - \frac{\pi}{8} \rho V^2 D^2 \times \begin{Bmatrix} C_{X0} + C_{X2}(v^2 + w^2)/V^2 \\ C_{NA}v/V - \frac{pD}{2V} C_{YPA}w/V \\ C_{NA}w/V + \frac{pD}{2V} C_{YPA}v/V \end{Bmatrix} \quad (8)$$

$$\begin{Bmatrix} L \\ M \\ N \end{Bmatrix} = \frac{\pi}{8} \rho V^2 D^3 \times \begin{Bmatrix} C_{LDD} + \frac{pD}{2V} C_{LP} \\ C_{MA} \frac{w}{V} + \frac{qD}{2V} C_{MQ} + \frac{pD}{2V} C_{NPA} \frac{v}{V} \\ -C_{MA} \frac{v}{V} + \frac{rD}{2V} C_{MQ} + \frac{pD}{2V} C_{NPA} \frac{w}{V} \end{Bmatrix} \quad (9)$$

The terms containing C_{YPA} constitute the Magnus air load acting at the Magnus center of pressure while the terms containing C_{X0} , C_{X2} , C_{NA} define the steady load acting at the center of pressure. The externally applied moment about the projectile mass center is composed of an unsteady aerodynamic moment along with terms due to the fact that the center of pressure and center of Magnus are not located at the mass center. The terms involving C_{MA} accounts for the center of pressure being located off the mass center while the terms involving

C_{NPA} accounts for the center of Magnus being located off the mass center. The aerodynamic coefficients are all a function of local Mach number which are typically handled through a table look-up scheme in projectile flight simulation codes. The aerodynamic model presented in equations (8) and (9) is the standard aerodynamic expansion for symmetric projectiles.

4 AERODYNAMIC COEFFICIENT ESTIMATION

The time accurate coupled CFD/RBD simulation provides a full flow solution including the aerodynamic portion of the total applied force and moment (X, Y, Z, L, M, N) along with the full state of the rigid projectile $(x, y, z, \phi, \theta, \psi, u, v, w, p, q, r)$ at every time step in the solution for each time snippet. Given a set of n short time histories (snippets) that each contain m time points yields a total of $h = m * n$ time history data points for use in estimating the aerodynamic coefficients: C_{X0} , C_{X2} , C_{NA} , C_{YPA} , C_{LDD} , C_{LP} , C_{MA} , C_{MQ} , C_{NPA} . Note that for fin-stabilized projectile configurations, the Magnus force and moment are usually sufficiently small so that C_{YPA} and C_{NPA} are set to zero and removed from the fitting procedure to be described below.

Equations (8) and (9) represent the applied air loads on the projectile expressed in the projectile body frame. Computation of the aerodynamic coefficients is aided by transforming these equations to the instantaneous aerodynamic angle of attack reference frame that rotates the projectile body frame about the \hat{I}_B axis by the angle $\gamma = \tan^{-1}(w/v)$.

$$-\frac{8}{\pi \rho V^2 D^2} \begin{bmatrix} 1 & 0 & 0 \\ 0 & c_\gamma & s_\gamma \\ 0 & -s_\gamma & c_\gamma \end{bmatrix} \begin{bmatrix} X \\ Y \\ Z \end{bmatrix} - W \begin{bmatrix} -s_\theta \\ s_\phi c_\theta \\ c_\phi c_\theta \end{bmatrix}$$

$$= \begin{Bmatrix} C_{X0} + C_{X2}(v^2 + w^2)/V^2 \\ C_{NA} \frac{\sqrt{v^2 + w^2}}{V} \\ \frac{pD}{2V} \frac{\sqrt{v^2 + w^2}}{V} C_{YPA} \end{Bmatrix} \quad (10)$$

$$\frac{8}{\pi \rho V^2 D^3} \begin{bmatrix} 1 & 0 & 0 \\ 0 & c_\gamma & s_\gamma \\ 0 & -s_\gamma & c_\gamma \end{bmatrix} \begin{bmatrix} L \\ M \\ N \end{bmatrix}$$

$$= \begin{Bmatrix} C_{LDD} + \frac{pD}{2V} C_{LP} \\ \frac{(vq + wr)D}{2\sqrt{v^2 + w^2}V} C_{MQ} + \frac{pD}{2V} \frac{\sqrt{v^2 + w^2}}{V} C_{NPA} \\ \frac{(vr - wq)D}{2\sqrt{v^2 + w^2}V} C_{MQ} - \frac{\sqrt{v^2 + w^2}}{V} C_{MA} \end{Bmatrix} \quad (11)$$

Each time history data point provides a total of six equations given by the components of equations (10) and (11). The first component of equation (10) is

gathered together for all time history data points to form equation (12). Likewise, the second and third components of equation (10) generate equations (13) and (14), respectively, while the first component of equation (11) constructs equation (15). Finally, the second and third components of equation (11) are gathered together to form equation (16). Subscripts on the projectile state vector and aerodynamic force and moment components represent the time history data point.

$$\begin{bmatrix} 1 & (v_1^2 + w_1^2)/V_1^2 \\ \vdots & \vdots \\ 1 & (v_h^2 + w_h^2)/V_h^2 \end{bmatrix} \begin{pmatrix} C_{X0} \\ C_{X2} \end{pmatrix} = \begin{bmatrix} -\frac{8}{\pi\rho V_1^2 D^2} (X_1 + W \sin \theta_1) \\ \vdots \\ -\frac{8}{\pi\rho V_h^2 D^2} (X_h + W \sin \theta_h) \end{bmatrix} \quad (12)$$

$$\begin{bmatrix} \sqrt{v_1^2 + w_1^2}/V_1 \\ \vdots \\ \sqrt{v_h^2 + w_h^2}/V_h \end{bmatrix} (C_{NA}) = \begin{bmatrix} -\frac{8}{\pi\rho V_1^2 D^2} (Y_1 \cos \gamma_1 + Z_1 \sin \gamma_1 - W \sin \phi_1 \cos \theta_1) \\ \vdots \\ -\frac{8}{\pi\rho V_h^2 D^2} (Y_h \cos \gamma_h + Z_h \sin \gamma_h - W \sin \phi_h \cos \theta_h) \end{bmatrix} \quad (13)$$

$$\begin{bmatrix} \frac{p_1 D \sqrt{v_1^2 + w_1^2}}{2V_1^2} \\ \vdots \\ \frac{p_h D \sqrt{v_h^2 + w_h^2}}{2V_h^2} \end{bmatrix} (C_{YPA}) = \begin{bmatrix} -\frac{8}{\pi\rho V_1^2 D^2} (-Y_1 \sin \gamma_1 + Z_1 \cos \gamma_1 - W \cos \phi_1 \cos \theta_1) \\ \vdots \\ -\frac{8}{\pi\rho V_h^2 D^2} (-Y_h \sin \gamma_h + Z_h \cos \gamma_h - W \cos \phi_h \cos \theta_h) \end{bmatrix} \quad (14)$$

$$\begin{bmatrix} 1 & \frac{p_1 D}{2V_1} \\ \vdots & \vdots \\ 1 & \frac{p_h D}{2V_h} \end{bmatrix} \begin{pmatrix} C_{LDD} \\ C_{LP} \end{pmatrix} = \begin{pmatrix} \frac{8L_1}{\pi\rho V_1^2 D^3} \\ \vdots \\ \frac{8L_h}{\pi\rho V_h^2 D^3} \end{pmatrix} \quad (15)$$

$$\begin{bmatrix} 0 & \frac{(v_1 q_1 + w_1 r_1)D}{2V_1 \sqrt{v_1^2 + w_1^2}} & \frac{p_1 D \sqrt{v_1^2 + w_1^2}}{2V_1^2} \\ -\frac{\sqrt{v_1^2 + w_1^2}}{V_1} & \frac{(v_1 r_1 - w_1 q_1)D}{2V_1 \sqrt{v_1^2 + w_1^2}} & 0 \\ \vdots & \vdots & \vdots \\ 0 & \frac{(v_h q_h + w_h r_h)D}{2V_h \sqrt{v_h^2 + w_h^2}} & \frac{p_h D \sqrt{v_h^2 + w_h^2}}{2V_h^2} \\ -\frac{\sqrt{v_h^2 + w_h^2}}{V_h} & \frac{(v_h r_h - w_h q_h)D}{2V_h \sqrt{v_h^2 + w_h^2}} & 0 \end{bmatrix} \times \begin{pmatrix} C_{MA} \\ C_{MQ} \\ C_{NPA} \end{pmatrix} = \begin{bmatrix} \frac{8}{\pi\rho V_1^2 D^3} (M_1 \cos \gamma_1 + N_1 \sin \gamma_1) \\ \frac{8}{\pi\rho V_1^2 D^3} (-M_1 \sin \gamma_1 + N_1 \cos \gamma_1) \\ \vdots \\ \frac{8}{\pi\rho V_h^2 D^3} (M_h \cos \gamma_h + N_h \sin \gamma_h) \\ \frac{8}{\pi\rho V_h^2 D^3} (-M_h \sin \gamma_h + N_h \cos \gamma_h) \end{bmatrix} \quad (16)$$

Equations (12) to (16) represent a set of five uncoupled problems to solve for the different aerodynamic coefficients. To estimate the aerodynamic coefficients near a particular Mach number, a set of n time accurate coupled CFD/RBD simulations are created over a relatively short time period. Since an individual time snippet is over a short time period where the projectile state variables do not change appreciably, it is critical that initial conditions for the different time snippet be selected in an informed way so that the rank of each of the fitting matrices above is maximal. Properties of the fitting matrices above, such as the rank or condition number, can be used as an indicator of the suitability of the CFD/RBD simulation data to estimate the aerodynamic coefficients at the target Mach number. Equation (12) is employed to estimate the zero yaw drag coefficient (C_{X0}) and the yaw drag coefficient (C_{X2}). To minimize the condition number of this fitting matrix, both low and high aerodynamic angle of attack time snippets are required. Equation (13) is used to compute the normal force coefficient (C_{NA}) and it requires time history data with a nonzero aerodynamic angle of attack. Equation (14) is used to compute the Magnus force coefficient (C_{YPA}) and it requires time history data with both low and high roll rate and aerodynamic angle of attack. Equation (15) is employed to estimate the fin cant roll coefficient (C_{LDD}) along with the roll damping coefficient (C_{LP}). To minimize the condition number of this fitting matrix, both low and

Table 1 Time snippet initial conditions

State	Case 1	Case 2	Case 3	Case 4
x (m)	0	0	0	0
y (m)	0	0	0	0
z (m)	0	0	0	0
ϕ (degrees)	0	0	0	0
θ (degrees)	0	0	0	0
ψ (degrees)	0	0	0	0
V (m/s)	1032	1032	1032	1032
v (m/s)	0	0	0	0
w (m/s)	0	-352.5	-90	0
P (rad/s)	0	0	377	0
q (rad/s)	0	0	0	-10
r (rad/s)	0	0	0	0
α (degrees)	0	20	5	0

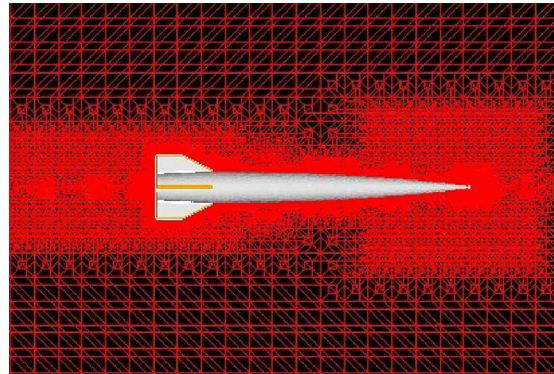
high roll rate time snippets are required. Equation (16) is employed to estimate the pitching moment coefficient (C_{MA}), the pitch damping coefficient (C_{MQ}), and the Magnus moment coefficient (C_{NPA}). For successful estimation of these coefficients, time history data with both low and high roll rate and aerodynamic angle of attack as well as low and high aerodynamic angle of attack are required. To meet the requirements for successful estimation of all five sets of aerodynamic coefficients, four time snippets are used all with different initial conditions. Table 1 lists the four cases with launch conditions. Notice that the set of time snippets contain a diverse set of initial conditions: zero aerodynamic angle of attack and angular rates; high angle of attack and zero angular rates; low angle of attack, high roll rate with other angular rates zero; zero angle of attack, high pitch rate with other angular rates zero.

For flight dynamic simulation, aerodynamic coefficients are required at a set of Mach numbers that covers the intended spectrum of flight conditions for the round. If aerodynamic coefficients are estimated at k different Mach numbers then a total of $l = k \times n$ CFD/RBD time snippets must be generated to construct the entire aerodynamic database for flight simulation purposes.

5 RESULTS

In order to exercise the method developed above, a generic finned projectile is considered. A sketch of the projectile is shown in Fig. 3. The projectile has the following geometric and mass properties: length = 0.1259 m, reference diameter = 0.013194 m, mass = 0.0484 kg, mass center location from base = 0.0686 m, roll inertia = $0.74e - 06$ kg m², pitch inertia = $0.484e - 04$ kg m².

As part of a validation of the coupled Navier-Stokes and six-degree-of-freedom method, time-accurate unsteady numerical computations were performed to predict the flow field, aerodynamic coefficients, and

**Fig. 3** Generic finned projectile**Fig. 4** Unstructured mesh near the finned body

the flight paths of this fin-stabilized projectile at an initial supersonic speed, $M = 3$. Full three-dimensional computations were performed and no symmetry was used.

An unstructured computational mesh was generated for the generic finned projectile (Fig. 4). In general, most of the grid points are clustered in the boundary-layer as well as near the afterbody fin and the wake regions. Three different grids were used and the total number of grid points varied from 2 to 6 million points for the full grid. For the larger meshes, additional grid points were clustered in the boundary-layer as well as near the afterbody fin and the wake regions. The first spacing away from the wall was selected to yield a y^+ value of 1.0 in each case. The projectile configuration has a base cavity and was included in the mesh generation process. The unstructured mesh also included the base cavity region that was present in the actual model tested and was generated using the multi-purpose intelligent meshing environment grid-generation software recently developed by Metacomp Technologies.

Here, the primary interest is in the validation of coupled CFD/RBD techniques for accurate simulation of free flight aerodynamics and flight dynamics of a projectile in supersonic flight. Numerical computations were made for the generic finned projectile configuration at an initial velocity of 1032 m/s. The initial angle of attack was, $\alpha = 4.9^\circ$ and initial spin rate was 2500 rad/s. Figure 5 shows the computed pressure contours at a given time or at a given location in the trajectory. It clearly shows the orientation of the body at that instant in time and the resulting asymmetric flow field due to the body at angle of attack.

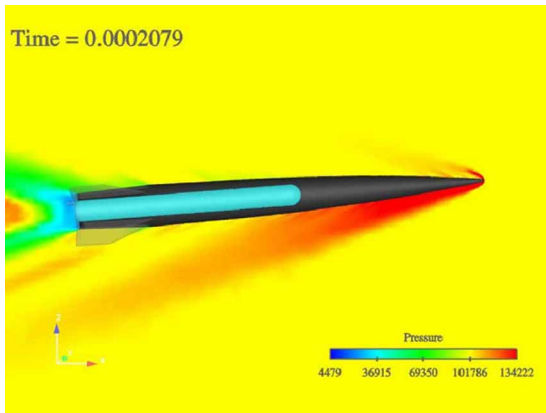


Fig. 5 Computed pressure contours

The orientation of the projectile of course changes from one instant in time to another as the projectile flies down range. Figure 6 shows the variation of the Euler pitch angle with distance traveled. As seen in this figure, both the amplitude and frequency in the Euler angle variation are predicted very well by the computed results and match extremely well with the data from the flight tests. One can also clearly see that the amplitude damps out as the projectile flies down range, i.e. with the increasing x -distance. Although not shown here, similar behavior is observed with the Euler yaw angle and it damps out with the increasing x -distance. Computed results again compare very well with measured data from flight tests. As stated earlier, different computational meshes were used to obtain the numerical results. Grid sizes varied from 2 to 6 million total number of points. The effect of the grid sizes on the computed Euler pitch angle is also shown in Fig. 6. The computed results are grid-independent;

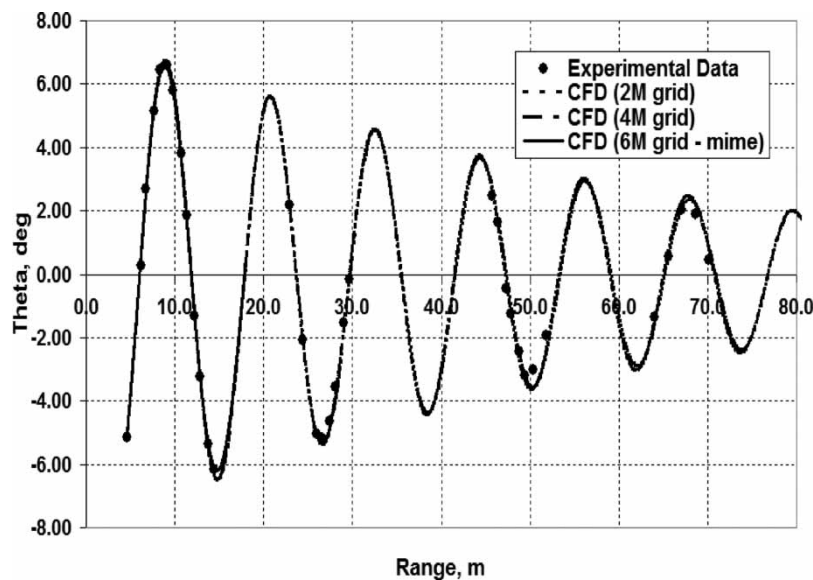


Fig. 6 Effect of mesh size on the Euler pitch angle

the computed pitch angles obtained with 4 and 6 million mesh are essentially the same as those results obtained with the 2 million point mesh. In all subsequent simulations, the 4 million grid point mesh has been used. Additional validation results showing other state variables and more details can be found in reference [34].

Figures 7 to 12 present projectile state trajectories for each of the four time snippets. Each time snippet is 0.023 s and contains 50 points, leading to an average output time step of 0.0004. The initial conditions for each of the time snippets is shown in Table 1. These four snippets create time history data at low and high angle of attack, roll rate, and pitch rate needed for accurate aerodynamic coefficient estimation. Notice that cases 2 and 3 have notably more drag down due to the high angle of attack launch conditions. Case 3 is launched with relatively high roll rate compared to all

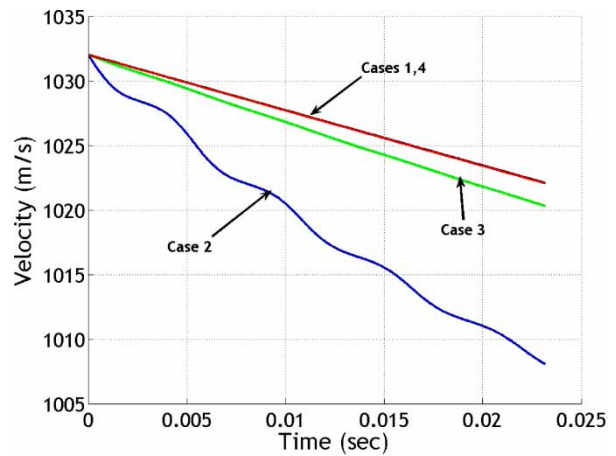


Fig. 7 Velocity for the time snippets.

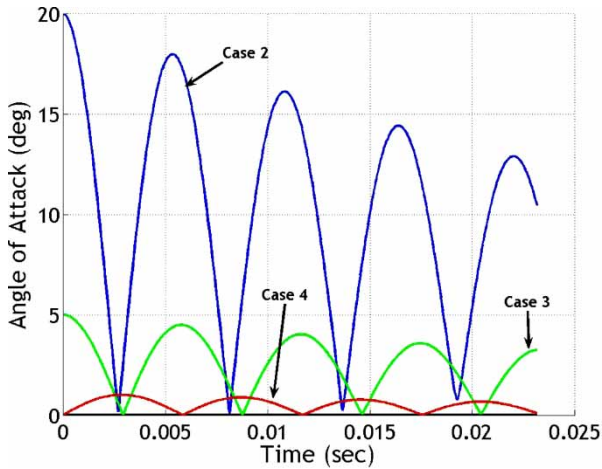


Fig. 8 Aerodynamic angle of attack for the time snippets

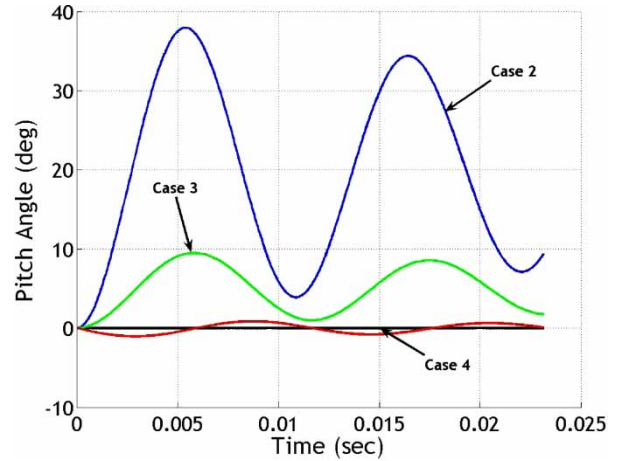


Fig. 11 Euler pitch angle for the time snippets

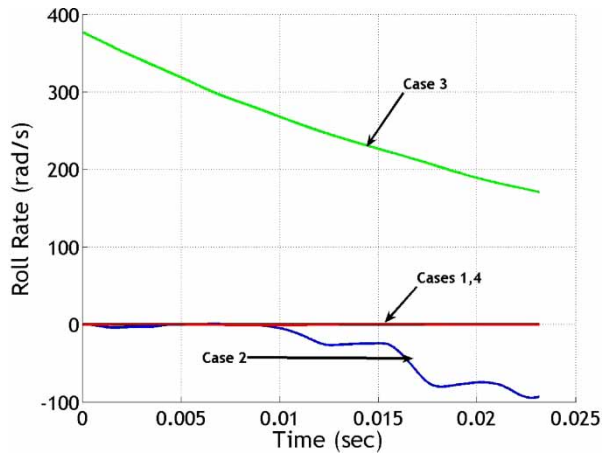


Fig. 9 Roll rate for the time snippets

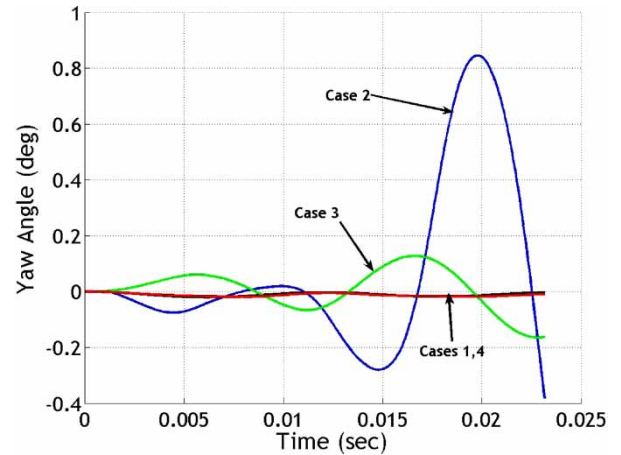


Fig. 12 Euler yaw angle for the time snippets

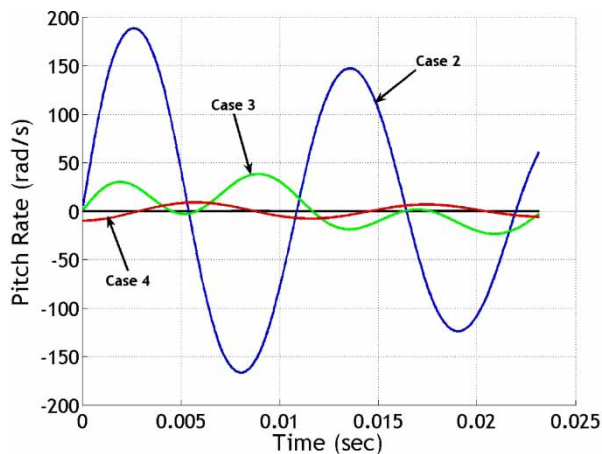


Fig. 10 Pitch rate for the time snippets

other cases. Case 2 generates roll rate toward the end of the time snippet due to high angle of attack roll-pitch coupling. Significant oscillations in Euler pitch angle are created in case 2 with some cross coupling response exhibited in Euler yaw angle. Figures 13 to 16 plot aerodynamic forces and moments in the local angle of attack reference frame defined above for cases 1, 3, and 4 since these cases are the primary cases used to estimate the coefficients. For all cases, the axial force oscillates from -20 to -25 N. There exists a slight bias between the CFD/RBD and estimated data of about 0.5 N for low angle of attack time snippets. For moderately high angles of attack (Case 3), the estimated data also oscillates with a much higher amplitude than the CFD/RBD data indicating that C_{x2} is estimated larger than the CFD/RBD suggests. The normal force time snippets agree well between the CFD/RBD and estimated data for all time snippets. For the example finned projectile, side force (F_z) and out-of-plane moment (M_y) are generally small (<0.5 N, 0.05 Nm) due to a negligibly small Magnus force and moment.

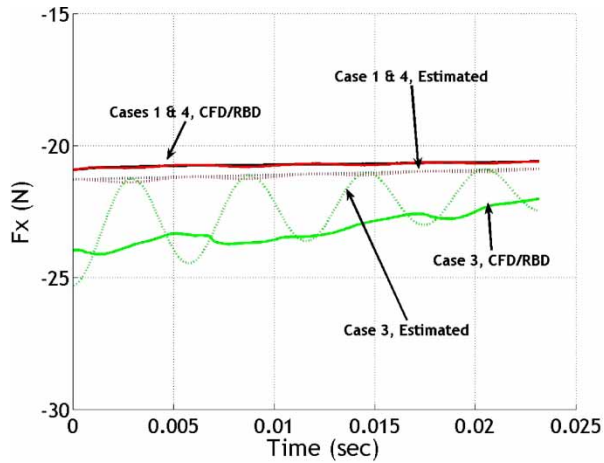


Fig. 13 Estimated (dashed) and CFD/RBD (solid) body axis axial force (F_x) versus time

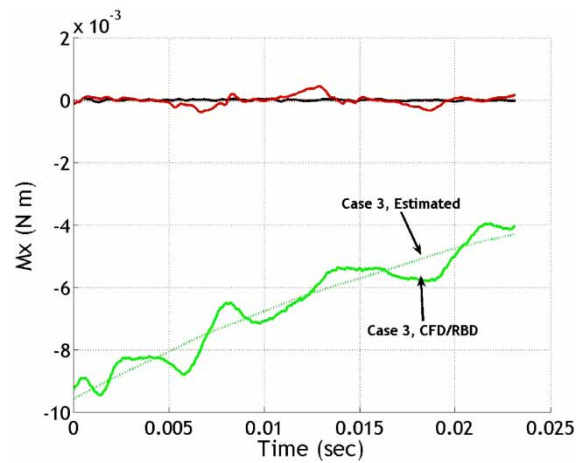


Fig. 15 Estimated (dashed) and CFD/RBD (solid) body axis rolling moment (M_x) versus time

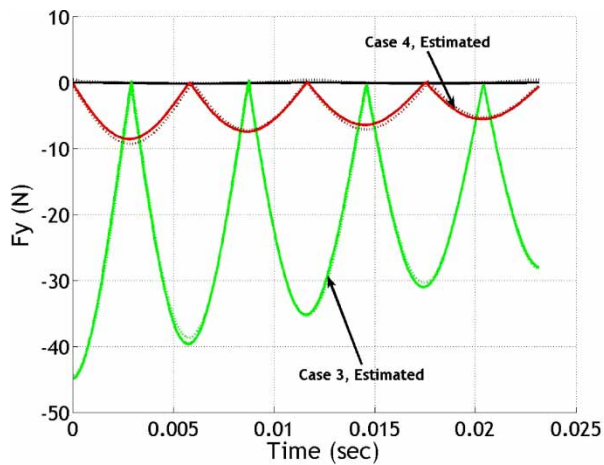


Fig. 14 Estimated (dashed) and CFD/RBD (solid) normal force (F_y) versus time

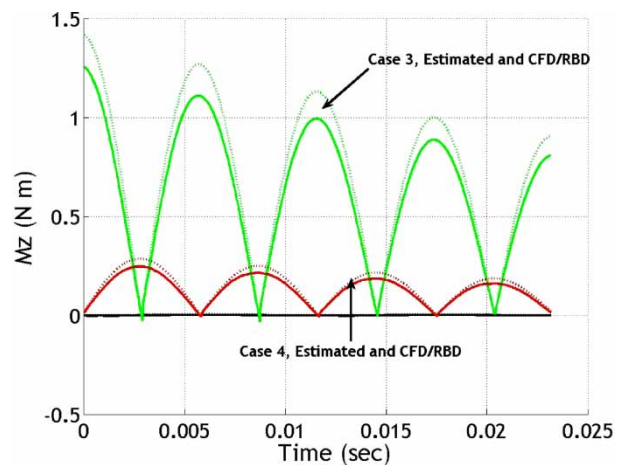


Fig. 16 Estimated (dashed) and CFD/RBD (solid) yawing moment versus time

The CFD/RBD and estimated data agree reasonably well, but certainly do not overlay one another. The only time snippet that creates notable rolling moment is case 3 which is launched with an initial roll rate of 377 rad/s. Notice that the estimated data smoothly goes through the CFD/RBD data which oscillates in a slightly erratic manner. The in-plane moment (M_z) agrees reasonably well for both the CFD/RBD and estimated data. The results shown in Figs 4 to 15 are typical for all Mach numbers. The overall observation from the data is that the estimated aerodynamic model fits the CFD/RBD data well, with the notable exception of axial force where a bias is exhibited.

The example projectile investigated in this paper has been fired in a spark range at Mach 3.0 with aerodynamic coefficients computed via conventional aerodynamic range reduction. Table 2 presents a comparison of aerodynamic coefficients obtained from spark range testing and subsequent coefficients

obtained using the method described here. Notice that most aerodynamic coefficients such as C_{X0} , C_{NA} , and C_{MA} are in reasonably good agreement with spark range reduced data. Axial force yaw drag and roll damping are both different by around 20 per cent while pitch damping is different by around 40 per cent. With the exception of C_{MQ} , aerodynamic coefficients are nearly estimated to within the accuracy that can be expected from a spark range test firing between two sets of firings. The relatively larger errors in C_{MQ} are more than likely due to the set of initial conditions that create a large condition number for the fitting matrix.

CFD/RBD data was generated at six different Mach numbers ranging from 1.5 to 4.0. The estimation algorithm discussed above was used to compute a complete set of aerodynamic coefficients across its Mach range. These results are provided in Table 3. With the exception of C_{X2} , the steady aerodynamic coefficients are smooth and follow typical trends for

Table 2 Comparison of estimated aerodynamic coefficients and estimated coefficients at Mach 3.0

	Spark range data– spark range reduction	CFD/RBD– PACE estimation	Percent difference between coefficients (%)
Zero yaw axial force coefficient, C_{X0}	0.221	0.238	7.1–7.7
Yaw axial force coefficient, C_{X2}	5.0	5.9	15.0–18.0
Normal force coefficient derivative, C_{NA}	5.83	5.64	3.2–3.3
Pitching moment coefficient derivative, C_{MA}	–12.6	–13.82	8.8–9.7
Pitch damping moment coefficient, C_{MQ}	–196	–134	31.6–46.3
Roll damping moment coefficient, C_{LP}	–2.71	–3.37	19.6–24.4

Table 3 Aerodynamic coefficients versus Mach number

Mach no.	1.5000	2.0000	2.5000	3.0000	3.5000	4.0000
C_{X0}	0.4309	0.3413	0.2821	0.2387	0.2051	0.1829
C_{X2}	0.2109	5.5363	5.7136	5.9329	5.5131	2.0191
C_{NA}	8.0982	7.0441	6.1940	5.6441	5.2608	5.0026
C_{LP}	–4.4758	–4.4114	–3.8793	–3.3788	–2.9415	–3.2974
C_{MA}	–23.7600	–18.6200	–15.7178	–13.8278	–12.4043	–11.3124
C_{MQ}	–282.8	–277.7	–182.3	–134.4	–112.0	–77.8

variation in Mach number. The yaw drag coefficient, C_{X2} , however, is somewhat erratic with a low value of 0.21 at Mach 1.5 followed by a steady rise until Mach 3.5. Pitch damping decreases with Mach number as would be expected for a fin-stabilized projectile beyond Mach 1.0. Roll damping steadily increases until Mach 4.0 when it drops off notably.

6 CONCLUSIONS

Using a time-accurate CFD simulation that is tightly coupled to a RBDs simulation, a method to efficiently generate a complete aerodynamic description for projectile flight dynamic modelling is described. A set of n short-time snippets of simulated projectile motion at m different Mach numbers is computed and employed as baseline data. The combined CFD/RBD analysis computes time synchronized air loads and projectile state vector information, leading to a straightforward fitting procedure to obtain the aerodynamic coefficients. The estimation procedure decouples into five sub problems that are each solved via linear least squares. The method has been applied to an example supersonic finned projectile. A comparison of spark range obtained aerodynamic coefficients with the estimation method presented here at Mach 3 exhibits agreement within 10 per cent for C_{X0} , C_{NA} , and C_{MA} ; agreement within 20 per cent for C_{X2} and C_{LP} ; and agreement within 40 per cent for C_{MQ} . This technique reported here provides a promising new means for the CFD analyst to predict aerodynamic coefficients for flight dynamic simulation purposes. It can easily be extended to flight dynamic modelling of different control effectors provided accurate CFD/RBD time simulation is possible and an aerodynamic coefficient

expansion is defined which includes the effect of the control mechanism.

REFERENCES

- Sun, J.** and **Cummings, R.** Evaluation of missile aerodynamic characteristics using rapid prediction techniques. *J. Spacecr. Rockets*, **21**(6), 513–520, 1984.
- Moore, F.** The 2005 version of the Aeroprediction Code (AP05). In the AIAA Atmospheric Flight Mechanics Conference, Providence, Rhode Island, 2004, AIAA paper 2004-4715.
- Sooy, T.** and **Schmidt, R.** Aerodynamic predictions, comparisons, and validations using missile DATCOM and aeroprediction 98. In the AIAA Aerospace Sciences Meeting and Exhibit, Reno, Nevada, 2004, AIAA paper 2004-1246.
- Simon, J.** and **Blake, W.** Missile DATCOM – high angle of attack capabilities. In the AIAA Atmospheric Flight Mechanics Conference, Portland, Oregon, 1999, AIAA paper 1999-4258.
- Neely, A.** and **Auman, I.** Missile DATCOM transonic drag improvements for hemispherical nose shapes. In the AIAA Applied Aerodynamics Conference, 2003, AIAA paper 2003-3668.
- Blake, W.** Missile DATCOM – 1997 status and future plans. In the AIAA Applied Aerodynamics Conference, Atlanta, Georgia, 1997, AIAA paper 1997-2280.
- Dupuis, A.** and **Berner, C.** Wind tunnel tests of a long range artillery shell concept. In the AIAA Atmospheric Flight Mechanics Conference, Monterey, California, 2002, AIAA paper 2002-4416.
- Berner, C.** and **Dupuis, A.** Wind tunnel tests of a grid fin projectile configuration. In the AIAA Aerospace Sciences Meeting, Reno, Nevada, 2001, AIAA paper 2001-0105.
- Evans, J.** Prediction of tubular projectile aerodynamics using the ZUES Euler code. *J. Spacecr. Rockets*, **1989**, **26**(5), 314–321.

- 10 **Sturek, W., Nietubicz, C., Sahu, J., and Weinacht, P.** Applications of computational fluid dynamics to the aerodynamics of army projectiles. *J. Spacecr. Rockets*, 1994, **31**(2), 186–199.
- 11 **Nusca, M., Chakravarthy, S., and Goldberg, U.** Computational fluid dynamics capability for the solid-fuel ramjet projectile. *J. Propuls. Power*, **6**(3), 1990, 256–262.
- 12 **Silton, S.** Navier-Stokes Computations for a spinning projectile from subsonic to supersonic speeds. *J. Spacecr. Rockets*, 2005, **42**(2), 223–231.
- 13 **DeSpirito, J., Vaughn, M., and Washington, D.** Numerical investigation of canard-controlled missile with planar grid fins. *J. Spacecr. Rockets*, 2003, **40**(3), 363–370.
- 14 **Sahu, J.** Numerical computations of transonic critical aerodynamic behavior. *AIAA J.*, 1990, **28**(5), 807–816.
- 15 **Weinacht, P.** Navier-Stokes prediction of the individual components of the pitch damping sum. *J. Spacecr. Rockets*, 1998, **35**(5), 598–605.
- 16 **Guidos, B., Weinacht, P., and Dolling, D.** Navier-Stokes computations for pointed, spherical, and flat tipped shells at Mach 3. *J. Spacecr. Rockets*, 1992, **29**(3), 305–311.
- 17 **Sahu, J. and Nietubicz, C. J.** Application of chimera technique to projectiles in relative motion. *J. Spacecr. Rockets*, 1995, **32**(5), 795–800.
- 18 **Park, S. and Kwon, J.** Navier-Stokes computations of stability derivatives for symmetric projectiles. In the AIAA Aerospace Sciences Meeting, Reno, Nevada, 2004, AIAA paper 2004-0014.
- 19 **Sahu, J.** Numerical simulations of supersonic flow over an elliptic-section projectile with jet-interaction. In the AIAA Aerodynamics Conference, St. Louis, MO, 24–27 June 2002, AIAA paper 2002-3260.
- 20 **Qin, N., Ludlow, K., Shaw, S., Edwards, J., and Dupuis, A.** Calculation of pitch damping for a flared projectile. *J. Spacecr. Rockets*, 1997, **34**(4), 566–568.
- 21 **Weinacht, P.** Coupled CFD/GN&C modeling for a smart material canard actuator. In the AIAA Atmospheric Flight Mechanics Conference, Providence, Rhode Island, 2004, AIAA paper 2004-4712.
- 22 **Park, S., Kim, Y., and Kwon, J.** Prediction of dynamic damping coefficients using unsteady dual time stepping method. In the AIAA Aerospace Sciences Meeting, Reno, Nevada, 2002, AIAA paper 2002-0715.
- 23 **DeSpirito, J. and Heavey, K.** CFD computation of Magnus moment and roll-damping moment of a spinning projectile. In the AIAA Atmospheric Flight Mechanics Conference, Providence, Rhode Island, 2004, AIAA paper 2004-4713.
- 24 **Sahu, J. and Heavey, K. R.** Unsteady CFD modeling of micro-adaptive flow control for an axisymmetric body. *Int. J. Comput. Fluid Dyn.*, 2006, **20**(5), 271–278.
- 25 **Garon, K., Abate, G., and Hathaway, W.** Free-flight testing of a generic missile with MEMs protuberances. In the AIAA Aerospace Sciences Meeting, Reno, Nevada, 2003, AIAA paper 2003-1242.
- 26 **Kruggel, B.** High angle of attack free flight missile testing. In the AIAA Aerospace Sciences Meeting, Reno, Nevada, 1999, AIAA paper 1999-0435.
- 27 **Danberg, J., Sigal, A., and Clemens, I.** Aerodynamic characteristics of a family of cone-cylinder-flare projectiles. *J. Spacecr. Rockets*, **27**(4), 1990.
- 28 **Dupuis, A.** Free-flight aerodynamic characteristics of a practice bomb at subsonic and transonic velocities. In the AIAA Atmospheric Flight Mechanics Conference, Monterey, California, 2002, AIAA paper 2002-4414.
- 29 **Abate, G., Duckerschein, R., and Hathaway, W.** Subsonic/transonic free-flight tests of a generic missile with grid fins. In the AIAA Aerospace Sciences Meeting, Reno, Nevada, 2000, AIAA paper 2000-0937.
- 30 **Chapman, G. and Kirk, D.** A method for extracting aerodynamic coefficients from free-flight data. *AIAA J.*, 1970, **8**(4), 753–758.
- 31 **Abate, G. and Klomfass, A.** Affect upon aeroballistic parameter identification from flight data errors. In the AIAA Aerospace Sciences Meeting, Reno, Nevada, 2005.
- 32 **Abate, G. and Klomfass, A.** A new method for obtaining aeroballistic parameters from flight data. In the Aeroballistic Range Association Meeting, Freiburg, Germany, 2004.
- 33 **Weinacht, P., Sturek, W., and Schiff, L.** Projectile performance, stability, and free-flight motion prediction using computational fluid dynamics. *J. Spacecr. Rockets*, 2004, **41**(20), 257–263.
- 34 **Sahu, J.** Time-accurate numerical prediction of free-flight aerodynamics of a finned projectile. In the AIAA Atmospheric Flight Mechanics Conference, San Francisco, California, 2005, AIAA paper 2005-5817.
- 35 **Etkin, B.** *Dynamics of atmospheric flight*, 1972 (John Wiley & Sons, USA).
- 36 **Peroomian, O., Chakravarthy, S., and Goldberg, U.** A 'grid-transparent' methodology for CFD. In the 35th Aerospace Sciences Meeting and Exhibit, Reno, Nevada, 1997, AIAA paper 97-07245.
- 37 **Peroomian, O., Chakravarthy, S., Palaniswamy, S., and Goldberg, U.** Convergence acceleration for unified-grid formulation using preconditioned implicit relaxation. In the 36th Aerospace Sciences Meeting and Exhibit, Reno, Nevada, 12–15 January 1998, AIAA paper 98-0116.
- 38 **Goldberg, U. C., Peroomian, O., and Chakravarthy, S.** A wall-distance-free K-E model with enhanced near-wall treatment. *ASME J. Fluids Eng.*, 1998, **120**, 457–462.
- 39 **Batten, P., Goldberg, U., and Chakravarthy, S.** Sub-grid turbulence modeling for unsteady flow with acoustic resonance. In Proceedings of the 38th AIAA Aerospace Sciences Meeting, Reno, Nevada, January 2000, AIAA paper 2000-0473.

APPENDIX

Notation

C_{LDD}	fin cant aerodynamic coefficient
C_{LP}	roll damping aerodynamic coefficient
C_{MQ}	pitch damping moment aerodynamic coefficient
C_{NA}	normal force due to angle of attack aerodynamic coefficient
C_{X0}	zero yaw drag aerodynamic coefficient
C_{X2}	yaw drag aerodynamic coefficient
C_{YPA}	Magnus force aerodynamic coefficient

D	projectile diameter	V	magnitude of relative aerodynamic velocity vector of mass center
F_x, F_y, F_z	total applied force components in body reference frame	W	projectile weight ($=mg$)
M_x, M_y, M_z	total applied moment components about mass center in body reference frame	x, y, z	components of position vector of mass center in an inertial reference frame
p, q, r	components of angular velocity vector in body reference frame	α	aerodynamic angle of attack
u, v, w	components of velocity vector of mass center in body reference frame	ρ	air density
		ϕ, θ, ψ	Euler roll, pitch, and yaw angles